Review of Modified Algorithms for Synthetic Aperture Radar Imaging at High Squint Angles

Po-Chih Chen and Jean-Fu Kiang

***Abstract*—This paper summarizes the modified versions of chirp scaling algorithm (CSA), range-Doppler algorithm (RDA) and frequency-domain algorithm (FDA) for synthetic aperture radar (SAR) imaging at high squint angles. The reviewed methods can reconstruct better images with less computational load and memory than their conventional counterparts, which is verified by simulations. SAR imaging with highly-elliptical-orbit (HEO) satellites based on these techniques is also reviewed.**

***Index Terms*—synthetic aperture radar (SAR), high squint angle, chirp scaling algorithm (CSA), range-Doppler algorithm (RDA), frequency-domain algorithm (FDA), highly-elliptical-orbit (HEO).**

I. Introduction

Synthetic aperture radar (SAR) techniques have been widely used to acquire high-resolution images of the ground. Many conventional SAR imaging algorithms work properly when the squint angle is small. However, as the squint angle becomes large, the slant range becomes a more complicated function of relevant geometrical parameters and the range-azimuth coupling also grows. To deal with such issues, more complicated algorithms were proposed, such as azimuth nonlinear chirp scaling (ANCS) [1], [2], frequency nonlinear chirp scaling (FNCS) [3], fractional CSA (FrCSA) [4], modified CSA [5], [6], range migration algorithm (RMA) [7], [8], improved step transform (IST) [9], azimuth overlapped subaperture algorithm (AOSA) [10], and so on.

At high squint angles, the range-Doppler spectrum resides on a very oblique subdomain and may fold in the Doppler-frequency dimension. A higher pulse repetition frequency (PRF) is required to remedy this issue [11], [12], which increases computational load and memory size. In addition, the difference between the maximum and the minimum slant ranges to the target area becomes very large, which demands larger matrices to store the received signals and the intermediate data, respectively [9]. In [13] and [14], modified SAR imaging algorithms were proposed to reduce the memory size by rotating the received baseband signals in the time domain to a new coordinate system in which the slant ranges at different slow times fall in similar ranges. The corresponding spectrum is also rotated to reside on a nearly rectangular subdomain, and the folded-spectrum problem is also resolved.

Inspired by these modified SAR imaging algorithms, highly-elliptical-orbit (HEO) satellites [15], [16], conventionally used for communications over high-latitude areas, are envisioned as platforms for SAR imaging. In [17], a constellation of two satellites in the Tundra orbit were simulated for SAR imaging. The Doppler centroid is extremely large when the satellite moves far away from the apogee, due to high eccentricity of the orbit, demanding a large number of samples along the slow-time dimension. In addition, the difference between the maximum and the minimum distances between the satellite and the target area is extremely large, demanding a much larger number of samples in the range dimension. Similar to the high-squint SAR scenarios, a modified frequency-domain algorithm (FDA) was proposed for the HEO SAR missions, which takes much smaller computational load and memory size than the conventional FDA.

This review paper is organized as follows. Four CSA-based methods [13], designed for spaceborne SAR imaging at high squint angles, are reviewed in Sections II; an RDA-based method [14] is reviewed in Sections III; an FDA-based method [17], tailored for HEO SAR imaging, is reviewed in Sections IV. Finally, a brief summary is presented in Section V.

II. CSA-Based Methods

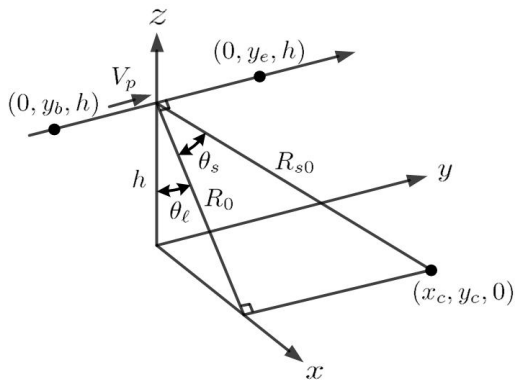

Fig. 1. Flight path of a platform carrying a SAR radar that points at a look angle θ_ℓ and a squint angle θ_s towards the target area [13].

Fig.1 shows the flight path of a platform carrying a SAR radar that points at a look angle θ_ℓ and a squint angle θ_s towards the target area [13]. The platform flies in the y direction from $(0, y_b, h)$ to $(0, y_e, h)$, at velocity of V_p and height of h. The beam center point (BCP) falls at $(x_c, y_c, 0)$, with $x_c = h\tan\theta_\ell$ and $y_c = h\tan\theta_s/\cos\theta_\ell$. The slant range from the center of the flight path to the BCP is $R_{s0} = \sqrt{x_c^2 + y_c^2 + h^2}$, and the range to the BCP is $R_0 = \sqrt{x_c^2 + h^2}$. At azimuth time η, the slant range from the platform to a point target at $(x, y, 0)$ is $R_s(\eta, x, y) = \sqrt{x^2 + (\eta V_p - y)^2 + h^2}$, and the range to the point target is $R(x) = \sqrt{x^2 + h^2}$.

P.-C. Chen and J.-F. Kiang are with the Graduate Institute of Communication Engineering, National Taiwan University, Taipei, Taiwan, ROC. E-mail: jfkiang@ntu.edu.tw.

A. Method A

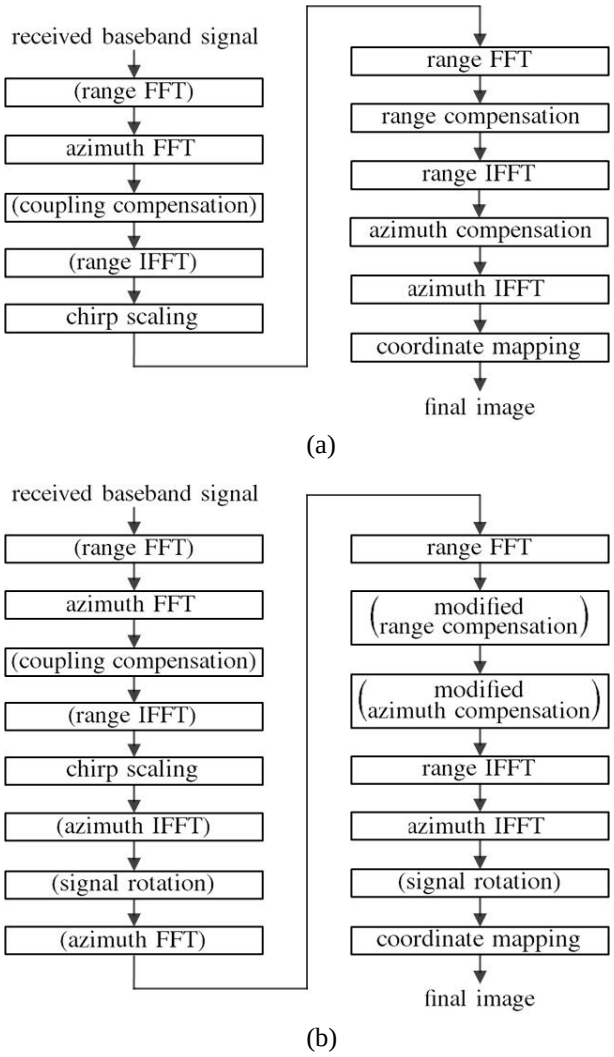

Fig. 2. Flowcharts of CSA-based methods for high-squint SAR imaging, (a) method A and (b) method B [13]. The processes enclosed with parentheses are different from those in the conventional CSA.

Fig.2(a) shows the flowchart of CSA, method A for high-squint SAR imaging [13], and the processes different from those in the conventional CSA are enclosed with parentheses [18]. The compensation of coupling is essential to high-squint SAR imaging, which is implemented in the two-dimensional frequency domain, requiring additional range FFT and range IFFT.

The transmitted linear frequency-modulation (LFM) signal is represented as $s_t(\tau) = w_e(\tau)e^{j2\pi f_0\tau + j\pi K_r\tau^2}$, where f_0 is the carrier frequency, K_r is the FM rate, τ is the range time, $w_e(\tau) = \mathrm{rect}(\tau/T_r)$ is the range envelope with duration T_r, and $\mathrm{rect}(\tau)$ is a rectangular function, which has unity amplitude in $|\tau| \le 1/2$ and zero otherwise. The demodulated scattering signal, at range time τ and azimuth time η, from a point target at $(x, y, 0)$ is expressed as

$$s_{\mathrm{rb}}(\tau,\eta) = A_0(x,y)w_e(\tau - 2R_s(\eta,x,y)/c) \\ e^{-j4\pi f_0 R_s(\eta,x,y)/c + j\pi K_r[\tau - 2R_s(\eta,x,y)/c]^2} \quad (1)$$

where $A_0(x,y)$ is a complex amplitude, which is arbitrarily set to one for convenience, and the radiation pattern from the SAR radar towards the point target is approximated as one.

Next, take the Fourier transform of the baseband signal in (1) with respect to τ and η to obtain

$$S_2(f_\tau, f_\eta) = c_1c_2A_0(x,y)W_e(f_\tau)e^{-j\pi f_\tau^2/K_r}e^{-j2\pi f_\eta(y/V_p)} \\ \exp\left\{-j\frac{4\pi R(x)f_0}{c}\sqrt{D^2 + \frac{2f_\tau}{f_0} + \frac{f_\tau^2}{f_0^2}}\right\} \quad (2)$$

where $W_e(f_\tau) = w_e(f_\tau/K_r)$, c_1 and c_2 are constants of integration, and $D = \sqrt{1 - \frac{c^2f_\eta^2}{4V_p^2f_0^2}}$. Typically, $D^2 \gg \left|\frac{2f_\tau}{f_0} + \frac{f_\tau^2}{f_0^2}\right|$, thus the square-root term in (2) can be approximated as

$$\sqrt{D^2 + \frac{2f_\tau}{f_0} + \frac{f_\tau^2}{f_0^2}} \simeq D + \frac{f_\tau}{Df_0} - \frac{c^2f_\eta^2f_\tau^2}{8D^3V_p^2f_0^4} + \frac{c^2f_\eta^2f_\tau^3}{8D^5V_p^2f_0^5} \quad (3)$$

As a comparison, only up to f_τ^2 terms are used in the conventional CSA. By substituting (3) into (2), we have

$$S_2(f_\tau, f_\eta) \simeq c_1c_2A_0(x,y)W_e(f_\tau)e^{-j\pi f_\tau^2/K_r}e^{-j2\pi f_\eta(y/V_p)} \\ \exp\left\{-j\frac{4\pi R(x)f_0}{c}\left[D + \frac{f_\tau}{Df_0} - \frac{c^2f_\eta^2f_\tau^2}{8D^3V_p^2f_0^4} + \frac{c^2f_\eta^2f_\tau^3}{8D^5V_p^2f_0^5}\right]\right\} \quad (4)$$

To compensate for the f_τ^3-term in the exponent of (4), a coupling compensation filter is devised as

$$H_{\mathrm{cc}}(f_\tau, f_\eta) = \exp\left\{j\frac{\pi\lambda_0R(x)f_\tau^3f_\eta^2}{2D^5f_0^3V_p^2}\right\}$$

which can be ignored in low-squint SAR imaging. The signal after applying the coupling compensation filter is inverse Fourier transformed with respect to f_τ to obtain

$$S_4(\tau, f_\eta) = c_1c_2c_3A_0(x,y)e^{-j2\pi f_\eta(y/V_p)} \\ w_e\left(\frac{1}{1 - K_rZ}\left[\tau - \frac{2R(x)}{cD}\right]\right)\exp\left\{-j\frac{4\pi R(x)f_0D}{c}\right\} \\ \exp\left\{j\pi K_m\left[\tau - \frac{2R(x)}{cD}\right]^2\right\} \quad (5)$$

where c_3 is a constant of integration, $K_m = \frac{K_r}{1 - K_rZ}$ and $Z = \frac{cR(x)f_\eta^2}{2D^3V_p^2f_0^3}$.

The slant range in the range-Doppler domain is decomposed as $r_s(R(x), f_\eta) = R(x)/D(f_\eta)$, and the total RCM of a point target is defined as $\mathrm{RCM}_t(R(x), f_\eta) = r_s(R(x), f_\eta) - r_s(R(x), f_{\eta_r})$, where f_{η_r} is commonly chosen at the Doppler centroid. The total RCM is further decomposed into a bulk RCM, $\mathrm{RCM}_b(f_\eta) = \mathrm{RCM}_t(R_r, f_\eta)$, determined at a reference range R_r, which is commonly chosen to be the range to the BCP, $R_0 = \sqrt{x_c^2 + h^2}$; as well as a differential RCM, $\mathrm{RCM}_d(R(x), f_\eta) = \mathrm{RCM}_t(R(x), f_\eta) - \mathrm{RCM}_b(f_\eta)$. The range time to the point target, after compensating the differential RCM, becomes $\tau = \frac{2}{c}[r_s(R(x), f_\eta) - \mathrm{RCM}_d(R(x), f_\eta)]$.

The range time to the reference point is $\tau_r = \frac{2}{c}[r_s(R_r, f_\eta)]$. The time shift associated with the differential RCM is $\Delta\tau = \frac{2}{c} \times \mathrm{RCM}_d(R(x), f_\eta) = \left[\frac{D(f_{\eta_r})}{D(f_\eta)} - 1\right]\tau'$, where $\tau' = \tau - \tau_r = \tau - \frac{2R_r}{cD(f_\eta)}$.

To compensate for the differential RCM, a chirp scaling function is devised as

$$H_{\mathrm{sc}}(\tau', f_\eta) = \exp\left\{j2\pi \int_0^{\tau'} f_{\mathrm{sc}}(u, f_\eta)du\right\}$$

where $f_{\mathrm{sc}}(u, f_\eta) = K_m \Delta\tau(u, f_\eta)$. If K_m is approximated as independent of range, the scaling function can be reduced to

$$H_{\mathrm{sc}}(\tau, f_\eta) = \exp\left\{j\pi K_m \left[\frac{D(f_{\eta_r})}{D} - 1\right]\left(\tau - \frac{2R_r}{cD}\right)^2\right\}$$

which is multiplied with (5) to derive a scaled signal in the range-Doppler domain as

$$\begin{aligned} S_5(\tau, f_\eta) = {} & c_1 c_2 c_3 A_0(x, y) e^{-j2\pi f_\eta (y/V_p)} \\ & w_e\left(\frac{1}{1 - K_r Z}\left[\tau - \frac{2R(x)}{cD}\right]\right) e^{-j4\pi R(x) f_0 D/c} \\ & \exp\left\{j\pi K_m \left[\tau - \frac{2R(x)}{cD}\right]^2\right\} \\ & \exp\left\{j\pi K_m \left[\frac{D(f_{\eta_r})}{D} - 1\right]\left(\tau - \frac{2R_r}{cD}\right)^2\right\} \end{aligned} \quad (6)$$

Next, by taking the Fourier transform of the scaled signal in (6) with respect to τ, and imposing the approximations that $Z \simeq 0$ and $f_{\eta_r} \simeq f_\eta$, we obtain

$$\begin{aligned} S_6(f_\tau, f_\eta) = {} & c_1 c_2 c_3 A_0(x, y) W_e(f_\tau) e^{-j2\pi f_\eta (y/V_p)} \\ & e^{-j4\pi R(x) f_0 D/c} \exp\left\{-j\frac{\pi D}{K_m D(f_{\eta_r})} f_\tau^2\right\} \\ & \exp\left\{\left(-j\frac{4\pi R(x)}{cD(f_{\eta_r})} - j\frac{4\pi R_r}{c}\left[\frac{1}{D} - \frac{1}{D(f_{\eta_r})}\right]\right) f_\tau\right\} \\ & \exp\left\{j\frac{4\pi K_m}{c^2}\left[\frac{R(x)}{D} - \frac{R_r}{D}\right]^2\left[1 - \frac{D}{D(f_{\eta_r})}\right]\right\} \end{aligned}$$

which is multiplied with a range-compensation filter

$$\begin{aligned} H_{\mathrm{rc}}(f_\tau, f_\eta) = {} & \exp\left\{j\frac{\pi D}{K_m D(f_{\eta_r})} f_\tau^2\right\} \\ & \exp\left\{j\frac{4\pi R_r}{c}\left[\frac{1}{D} - \frac{1}{D(f_{\eta_r})}\right] f_\tau\right\} \end{aligned} \quad (7)$$

to derive

$$\begin{aligned} S_7(f_\tau, f_\eta) = {} & c_1 c_2 c_3 A_0(x, y) W_e(f_\tau) e^{-j2\pi f_\eta (y/V_p)} \\ & e^{-j4\pi R(x) f_0 D/c} \exp\left\{-j\frac{4\pi R(x)}{cD(f_{\eta_r})} f_\tau\right\} \\ & \exp\left\{j\frac{4\pi K_m}{c^2}\left[\frac{R(x)}{D} - \frac{R_r}{D}\right]^2\left[1 - \frac{D}{D(f_{\eta_r})}\right]\right\} \end{aligned}$$

which is then inverse Fourier transformed with respect to f_τ to have

$$\begin{aligned} S_8(\tau, f_\eta) = {} & c_1 c_2 c_3 A_0(x, y) e^{-j2\pi f_\eta (y/V_p)} e^{-j4\pi R(x) f_0 D/c} \\ & \exp\left\{j\frac{4\pi K_m}{c^2}\left[\frac{R(x)}{D} - \frac{R_r}{D}\right]^2\left[1 - \frac{D}{D(f_{\eta_r})}\right]\right\} \\ & F_r \mathrm{sinc}\left\{F_r\left[\tau - \frac{2R(x)}{cD(f_{\eta_r})}\right]\right\} \end{aligned}$$

with $-F_r/2 < f_\tau < F_r/2 - F_r/N_r$, where F_r is the range sampling rate.

By applying an azimuth-compensation filter

$$H_{\mathrm{ac}}(f_\eta) = \exp\left\{j\frac{4\pi R(x) f_0 D}{c}\right\} \quad (8)$$

and a residual-phase compensation filter

$$H_{\mathrm{rpc}}(f_\eta) = \exp\left\{-j\frac{4\pi K_m}{c^2}\left[\frac{R(x)}{D} - \frac{R_r}{D}\right]^2\left[1 - \frac{D}{D(f_{\eta_r})}\right]\right\} \quad (9)$$

to $S_8(\tau, f_\eta)$, we obtain

$$\begin{aligned} S_9(\tau, f_\eta) = {} & c_1 c_2 c_3 A_0(x, y) e^{-j2\pi f_\eta (y/V_p)} \\ & F_r \mathrm{sinc}\left\{F_r\left[\tau - \frac{2R(x)}{cD(f_{\eta_r})}\right]\right\} \end{aligned}$$

which is inverse Fourier transformed with respect to f_η to obtain

$$\begin{aligned} s_{10}(\tau, \eta) = {} & c_1 c_2 c_3 A_0(x, y) F_r \mathrm{sinc}\left\{F_r\left[\tau - \frac{2R(x)}{cD(f_{\eta_r})}\right]\right\} \\ & F_a \mathrm{sinc}\left\{F_a\left(\eta - y/V_p\right)\right\} \end{aligned} \quad (10)$$

with $-F_a/2 < f_\eta < F_a/2 - F_a/N_a$, where F_a is the azimuth sampling rate. Based on (10), the τ-η coordinates of the point target are estimated as $\tau = \frac{2R(x)}{cD(f_{\eta_r})}$ and $\eta = \frac{y}{V_p}$, which are mapped to $x = \sqrt{\left[\frac{cD(f_{\eta_r})\tau}{2}\right]^2 - h^2}$ and $y = V_p\eta$

B. Method B

Fig.2(b) shows the flowchart of CSA, method B for high-squint SAR imaging. The processes before chirp scaling remain the same as in method A. A two-dimensional similarity theorem is applied to reduce computational load and memory size, which states that if the signals in the τ-η plane is rotated by a given angle, the corresponding Fourier-transformed signals in the f_τ-f_η plane will be rotated by the same angle.

The received baseband signals, represented in (1), are stored in a matrix of dimension $N_a \times N_r$, where the azimuth sampling number (N_a) determines the resolution in the azimuthal direction, and the range sampling number (N_r) must be large enough to store all the scattered signals from the target area. For the convenience of applying the FFT algorithm, both N_a and N_r are incremented, respectively, to the nearest integers that are powers of two.

Figs.3(a) and 3(b) show the storage areas of received baseband signals in $(\tau - \tau_0, \eta)$ plane and $(\tau' - \tau_0, \eta')$ plane,

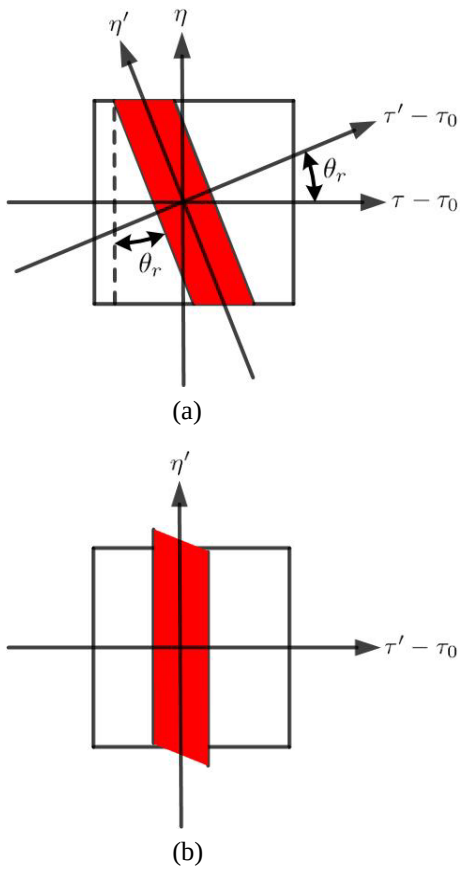

Fig. 3. Storage area of received baseband signals in (a) $(\tau - \tau_0, \eta)$ plane and (b) $(\tau' - \tau_0, \eta')$ plane.

respectively, where $\tau_0 = 2R_{s0}/c$. The number of range samples in Fig.3(b) is much smaller than that in Fig.3(a). The rotation angle θ_r between these two coordinate systems is chosen as $\theta_r = \tan^{-1}\dfrac{2D/c}{L/V_p}$, where $L = y_e - y_b$ is the total length of the flight path, and $D = \sqrt{x_c^2 + (y_c - y_b)^2 + h^2} - \sqrt{x_c^2 + (y_c - y_e)^2 + h^2}$ is the length difference between the two line segments that connect the BCP to the starting point and ending point, respectively, of the flight path. Explicitly, the $(\tau - \tau_0, \eta)$ coordinates are related to the $(\tau' - \tau_0, \eta')$ coordinates as

$$\begin{bmatrix} \tau \\ \eta \end{bmatrix} = \begin{bmatrix} (\tau' - \tau_0)\cos\theta_r - \eta' \sin\theta_r + \tau_0 \\ (\tau' - \tau_0)\sin\theta_r + \eta' \cos\theta_r \end{bmatrix} = \begin{bmatrix} g(\tau', \eta') \\ h(\tau', \eta') \end{bmatrix} \tag{11}$$

By taking an inverse Fourier transform of the scaled signal in (6) with respect to f_η, we have

$$s_{\rm sc}(\tau, \eta) = \mathcal{F}_\eta^{-1}\{S_5(\tau, f_\eta)\}$$

The scaled signals in the (τ, η) coordinates can now be represented in the (τ', η') coordinates as

$$s_{\rm sc}(\tau', \eta') = s_{\rm sc}(\tau, \eta)\Big|_{\tau = g(\tau', \eta'), \eta = h(\tau', \eta')}$$

TABLE I
PARAMETERS OF SAR MISSION [18].

parameter	symbol	magnitude	unit
effective radar velocity	V_p	7,100	m/s
carrier frequency	f_0	5.3	GHz
chirp pulse duration	T_r	40	μs
range chirp rate	K_r	500	GHz/s
bandwidth	B_r	20	MHz
range sampling rate	F_r	96 / 24*	MHz
range sampling interval	$\Delta\tau$	10.42 / 41.67*	ns
number of range samples	N_r	16,384	
azimuth sampling rate	F_a	6,800 / 1,700*	Hz
azimuth sampling interval	$\Delta\eta$	0.15 / 0.59*	ms
number of azimuth samples	N_a	16,384	
height of the platform	h	800	km
look angle	θ_ℓ	19.75	deg.
squint angle	θ_s	60 / 80*	deg.

* a/b: a is used at $\theta_s = 60^\circ$ and b is used at $\theta_s = 80^\circ$.

which are stored in a matrix of dimension $N_a' \times N_r'$. Without loss of generality, we choose $\Delta\tau' = \Delta\tau$ and $\Delta\eta' = \Delta\eta$.

The filters $H_{\rm ac}(f_\eta)$ in (8) and $H_{\rm rpc}(f_\eta)$ in (9) can be relabeled as $H_{\rm ac}(f_\tau, f_\eta)$ and $H_{\rm rpc}(f_\tau, f_\eta)$, respectively. Both filters and the range-compensation filter in (7) can be represented in the f_τ'-f_η' plane as

$$H_{\rm rc}(f_\tau', f_\eta') = H_{\rm rc}(f_\tau, f_\eta)\Big|_{f_\tau = g_1(f_\tau', f_\eta'), f_\eta = h_1(f_\tau', f_\eta')}$$

$$H_{\rm ac}(f_\tau', f_\eta') = H_{\rm ac}(f_\tau, f_\eta)\Big|_{f_\tau = g_1(f_\tau', f_\eta'), f_\eta = h_1(f_\tau', f_\eta')}$$

$$H_{\rm rpc}(f_\tau', f_\eta') = H_{\rm rpc}(f_\tau, f_\eta)\Big|_{f_\tau = g_1(f_\tau', f_\eta'), f_\eta = h_1(f_\tau', f_\eta')}$$

where $(f_\tau, f_\eta - f_{\rm dc})$ are related to $(f_\tau', f_\eta' - f_{\rm dc})$ by the same rotational matrix in (11) as

$$\begin{bmatrix} f_\tau \\ f_\eta \end{bmatrix} = \begin{bmatrix} f_\tau' \cos\theta_r - (f_\eta' - f_{\rm dc})\sin\theta_r \\ f_\tau' \sin\theta_r + (f_\eta' - f_{\rm dc})\cos\theta_r + f_{\rm dc} \end{bmatrix} = \begin{bmatrix} g_1(f_\tau', f_\eta') \\ h_1(f_\tau', f_\eta') \end{bmatrix}$$

C. Methods C and D

Method C is revised from method A by implementing the range-compensation process right after the coupling-compensation process, eliminating a range FFT and a range IFFT processes. Method D inherits the advantage of reduced memory storage in method B and implements the range-compensation process right after the coupling-compensation process, as in method C. In addition, the coupling compensation filter is implemented in the rotated coordinates, further reducing the computational load.

Two missions with squint angles of 60° and 80°, respectively, are simulated to verify the efficacy of these methods.

D. Mission with $\theta_s = 60^\circ$

Table I lists the parameters of SAR missions simulated in this work [18]. Fig.4(a) shows the received signals, computed

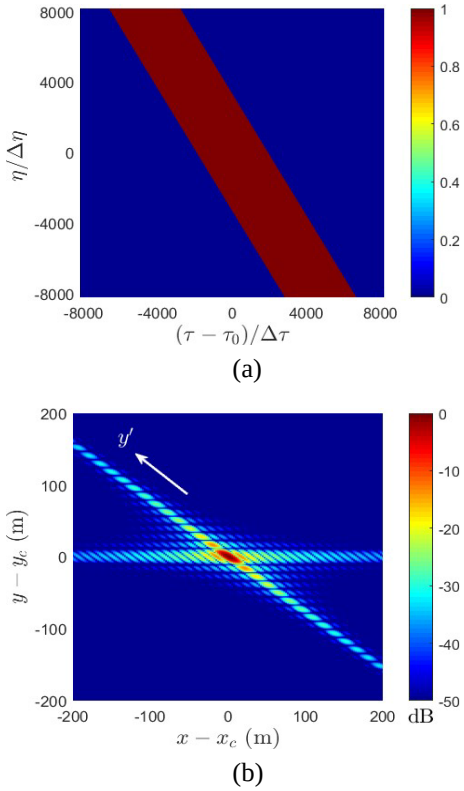

Fig. 4. (a) Received signals in τ-η plane and (b) image reconstructed with method A, $\theta_s = 60°$, $N_r = 16,384$, $N_a = 16,384$ [13].

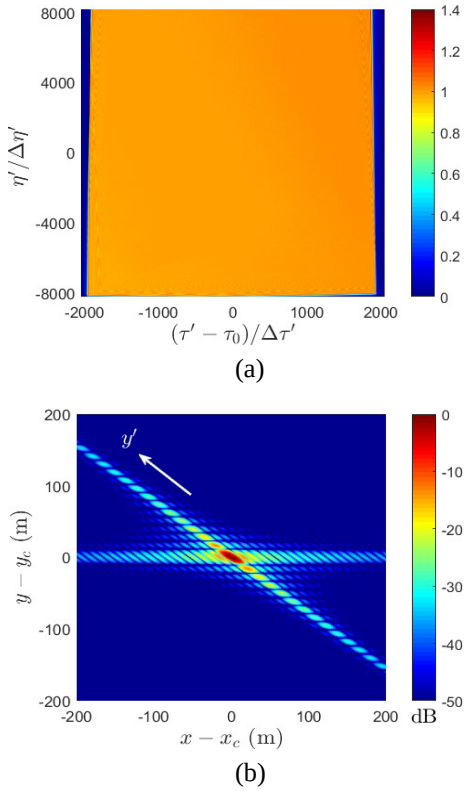

Fig. 5. (a) Scaled signals in τ'-η' plane and (b) image reconstructed with method B, $\theta_s = 60°$, $N'_r = 4,096$, $N'_a = 16,384$ [13].

TABLE II
PERFORMANCE INDICES OF SAR IMAGING, $\theta_s = 60°$ [13].

index	method A	method B	method C	method D
IRW$_x$ (m)	9.6926	9.7044	9.7518	9.741
PSLR$_x$ (dB)	-13.2483	-13.3807	-13.2082	-13.2435
ISLR$_x$ (dB)	-9.8324	-9.8727	-9.6109	-9.6539
TO$_x$ (m)	-1.0139	0.6690	-1.0139	0.6690
IRW$_{y'}$ (m)	15.8738	16.1828	15.8711	16.1835
PSLR$_{y'}$ (dB)	-13.3249	-13.2313	-13.3439	-13.2461
ISLR$_{y'}$ (dB)	-10.6284	-9.7876	-9.8878	-9.8111
TO$_{y'}$ (m)	0.5221	-0.5221	-0.5221	-0.5221
NOM (million)	48,050	42,480	33,018	27,313
memory (GB)	4	1	4	1

by using (1), in the τ-η plane. Fig.4(b) shows the image reconstructed with method A, in which local maxima are observed along the x axis and a y' axis.

Fig.5(a) shows the scaled signals in the τ'-η' plane, and Fig.5(b) shows the image reconstructed with method B. The number of range samples is reduced to $N'_r = 4,096$, and the number of azimuth samples remains as $N'_a = 16,384$. The image reconstructed with method B appears similar to that with method A. The memory required by method A to store the received signals is on the order of $N_r \times N_a$, while that required by method B is on the order of $N'_r \times N'_a$. The reconstructed images with methods C and D also appear similar to those obtained with methods A and B.

Table II lists the performance indices of SAR imaging by using different methods, with $\theta_s = 60°$. The impulse response width (IRW) is defined as the separation between two half-power points, one on each side of the peak-intensity point; the peak sidelobe ratio (PSLR) is the ratio between the peak intensity and that of the strongest sidelobe; the integrated sidelobe ratio (ISLR) is the ratio between the total intensity in the main-lobe and that in all the sidelobes; and the target offset (TO) is the offset of the peak-intensity point in the reconstructed image from the actual point target. The images reconstructed with these four methods have similar IRW, PSLR, ISLR and TO, in both x and y' directions. However, methods B and D take only 25 % of memory as compared to methods A and C, due to the signal-rotation scheme. The numbers of multiplications (NOMs) required by methods A, B, C and D have the ratio of $1 : 0.884 : 0.687 : 0.568$. In summary, method D out-performs the other three in NOMs and memory.

E. Mission with $\theta_s = 80°$

Fig.6 shows the image reconstructed by using method A, with $\theta_s = 80°$. When method B is applied, the number of range samples is reduced to $N'_r = 1,024$, and that of azimuth samples remains as $N'_a = 16,384$. Table III lists the performance indices of SAR imaging by using different methods, with $\theta_s = 80°$. The IRWs in the x direction (IRW$_x$) with methods A and B are smaller than those with methods C and D. The images reconstructed with these four methods have similar IRW$_{y'}$, PSLR$_{y'}$, ISLR$_{y'}$, TO$_x$ and TO$_{y'}$. However, methods B and D take only 6.25 % of memory as compared to methods A and C, due to the signal-rotation scheme. The NOMs required by methods A, B, C and D have the ratio

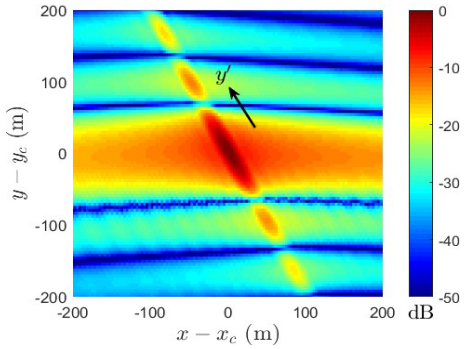

Fig. 6. Image reconstructed with method A, $\theta_s = 80°$, $N_r = 16,384$, $N_a = 16,384$ [13].

TABLE III
PERFORMANCE INDICES OF SAR IMAGING, $\theta_s = 80°$ [13].

index	method A	method B	method C	method D
IRW_x (m)	17.3514	17.2602	23.1362	23.1751
TO_x (m)	1.5876	1.0568	1.5876	−1.0568
$\text{IRW}_{y'}$ (m)	66.2745	66.9248	66.1876	66.6461
$\text{PSLR}_{y'}$ (dB)	−12.9808	−13.216	−13.0324	−13.2466
$\text{ISLR}_{y'}$ (dB)	−11.3791	−10.0151	−11.3496	−9.8239
$\text{TO}_{y'}$ (m)	−2.0882	2.0882	−2.0882	2.0882
NOM (million)	48,050	34,014	33,018	18,572
memory (GB)	4	0.25	4	0.25

of $1 : 0.708 : 0.687 : 0.387$. In summary, method D outperforms the other three in NOMs and memory, but is poorer than methods A and B in IRW_x.

III. RDA-BASED METHOD

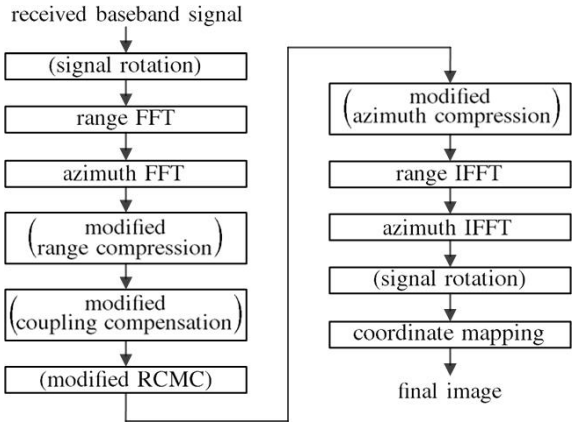

Fig. 7. Flowchart of RDA-based method for high-squint SAR imaging [14]. The processes enclosed with parentheses are different from those in the conventional RDA [18].

Fig.7 shows the flowchart of an RDA-based method for high-squint SAR imaging [14]. To begin with, the time-domain received baseband signals are rotated to a new coordinate system. Two major processes, range compression and azimuth compression, are implemented in the f_τ-f_η domain. Four relevant filters are applied in the two-dimensional frequency domain after rotation. At last, the processed signals are rotated back to the τ-η domain and mapped to the x-y coordinates.

The received baseband signals stored in the (τ, η) coordinates are transformed to the (τ', η') coordinates as

$$s_{\text{rb}}(\tau', \eta') = s_{\text{rb}}(\tau, \eta)\Big|_{\tau=g(\tau',\eta'),\eta=h(\tau',\eta')} \tag{12}$$

which are interpolated to a uniform grid in the τ'-η' plane and stored in a matrix of dimension $N_a' \times N_r'$. Without loss of generality, we choose $\Delta\tau' = \Delta\tau$ and $\Delta\eta' = \Delta\eta$. The range-compression filter used in the conventional RDA is [19]

$$H_{\text{rc}}(f_\tau, f_\eta) = e^{j\pi f_\tau^2/K_m}$$

where

$$\frac{1}{K_m} = \frac{1}{K_r} - \frac{\lambda_0 R(x) f_\eta^2}{2D^3 f_0^2 V_p^2}$$

$$D = D(f_\eta) = \sqrt{1 - \frac{c^2 f_\eta^2}{4 f_0^2 V_p^2}}$$

which is applied in the f_τ-f_η domain instead of the f_τ-η domain as in the conventional RDA. An azimuth-compression filter is devised as [19]

$$H_{\text{ac}}(f_\tau, f_\eta) = e^{j4\pi R(x) D/\lambda_0}$$

which is applied in the f_τ-f_η domain instead of the τ-f_η domain as in the conventional RDA. A range cell migration correction (RCMC) filter is devised as [19]

$$H_{\text{rcmc}}(f_\tau, f_\eta) = \exp\left\{ j \frac{4\pi R(x) f_\tau}{c} \left[\frac{1}{D} - \frac{1}{D(f_{\text{dc}})} \right] \right\}$$

At high squint angles, a coupling-compensation filter is required [19]

$$H_{\text{cc}}(f_\tau, f_\eta) = \exp\left\{ j \frac{\pi \lambda_0 R(x) f_\tau^3 f_\eta^2}{2D^5 f_0^3 V_p^2} \right\}$$

These four filters are rotated to the f_τ'-f_η' plane as

$$H_{\text{rc}}(f_\tau', f_\eta') = H_{\text{rc}}(f_\tau, f_\eta)\Big|_{f_\tau=g_1(f_\tau',f_\eta'),f_\eta=h_1(f_\tau',f_\eta')}$$

$$H_{\text{cc}}(f_\tau', f_\eta') = H_{\text{cc}}(f_\tau, f_\eta)\Big|_{f_\tau=g_1(f_\tau',f_\eta'),f_\eta=h_1(f_\tau',f_\eta')}$$

$$H_{\text{rcmc}}(f_\tau', f_\eta') = H_{\text{rcmc}}(f_\tau, f_\eta)\Big|_{f_\tau=g_1(f_\tau',f_\eta'),f_\eta=h_1(f_\tau',f_\eta')}$$

$$H_{\text{ac}}(f_\tau', f_\eta') = H_{\text{ac}}(f_\tau, f_\eta)\Big|_{f_\tau=g_1(f_\tau',f_\eta'),f_\eta=h_1(f_\tau',f_\eta')}$$

Two missions with squint angles of 60° and 80°, respectively, are simulated to verify the efficacy of this method.

A. Mission with $\theta_s = 60°$

The same parameters of SAR missions, as listed in Table I, are used in the simulations [18]. Fig.8(a) shows the received signal in the τ-η plane, computed by using (1). Fig.8(b) shows the image reconstructed with the conventional RDA, in which local maxima are observed along the x axis and a y' axis.

Fig.9(a) shows the received signal in the τ'-η' plane, computed by using (12); and Fig.9(b) shows the image reconstructed with the RDA-based method. The number of range

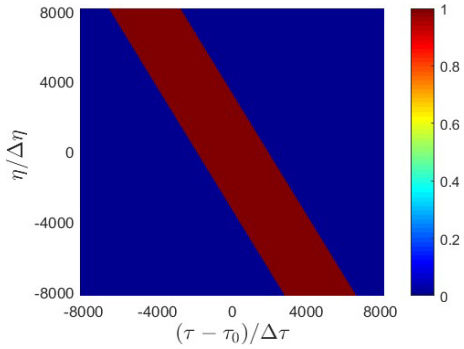

(a)

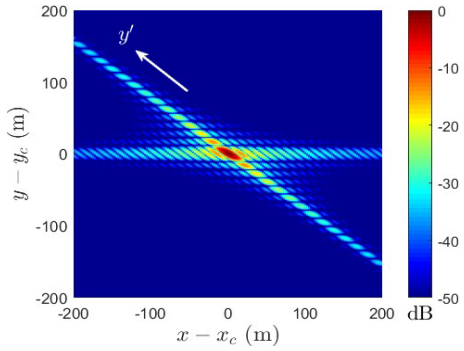

(b)

Fig. 8. (a) Received signal in τ-η plane and (b) image reconstructed with the conventional RDA, $\theta_s = 60°$, $N_r = 16,384$, $N_a = 16,384$ [14].

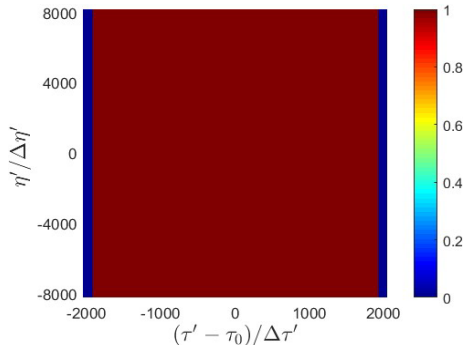

(a)

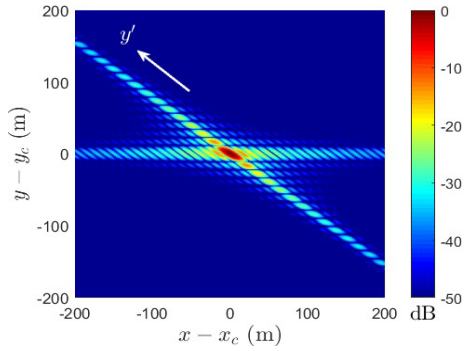

(b)

Fig. 9. (a) Received signal in τ'-η' plane and (b) image reconstructed with the RDA-based method in scheme A, $\theta_s = 60°$, $N'_r = 4,096$, $N'_a = 16,384$ [14].

TABLE IV
PERFORMANCE INDICES OF IMAGING SAR, $\theta_s = 60°$ [14].

index	conventional	scheme A	scheme B
IRW$_x$ (m)	9.6928	9.6833	9.6826
PSLR$_x$ (dB)	-13.2521	-13.2418	-13.2406
IRW$_{y'}$ (m)	16.3341	16.1536	8.1589
PSLR$_{y'}$ (dB)	-13.3216	-13.2337	-13.1988
NOM (million)	35,165	11,542	23,622
memory (GB)	4	1	2

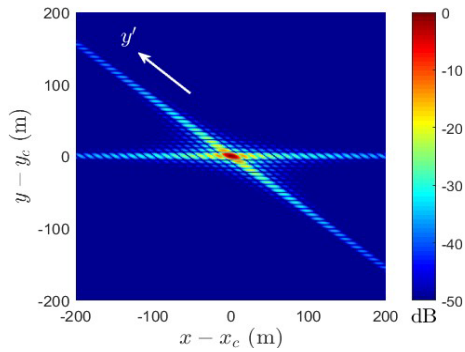

Fig. 10. Image reconstructed with RDA-based method, scheme B, $\theta_s = 60°$, $N'_r = 4,096$, $N'_a = 32,768$ [14].

samples is reduced to $N'_r = 4,096$, and the number of azimuth samples remains as $N'_a = 16,384$. This scenario is labeled as scheme A. The image reconstructed with the RDA-based method appears similar to that with the conventional RDA. The memory required by the conventional RDA and the RDA-based method to store the received signals are on the order of $N_r \times N_a$ and $N'_r \times N'_a$, respectively.

A second set of parameters, $N'_r = 4,096$ and $N'_a = 32,768$, are chosen to form scheme B. The number of range samples is the same as that in scheme A, but that of the azimuth samples is doubled. The NOMs and memory required in scheme B are larger than that in scheme A. Fig.10 shows the image reconstructed with the RDA-based method. The number of range samples required is only a quarter that required by the conventional RDA, and the number of azimuth samples is twice that of the conventional RDA. The reconstructed image appears to have finer spatial resolution in the y' direction because the synthetic aperture length is doubled.

Table IV lists the performance indices of SAR imaging by using the RDA-based method, with $\theta_s = 60°$. The images reconstructed with the conventional RDA and the RDA-based method in scheme A are similar. However, the latter takes only 33 % of NOMs and 25 % of memory as compared to the former. The spatial resolutions in the x direction with the conventional RDA and the RDA-based method are similar in both schemes, and the spatial resolution in the y' direction with the latter in scheme B is only half that with the former. The RDA-based method in scheme B takes 205 % of NOMs and twice memory as compared to those in scheme A. However, the former takes only 67 % of NOMs and one half memory as compared to the conventional RDA. In summary, the RDA-based method in scheme B out-performs the conventional RDA in spatial resolution along y' direction, NOMs and memory.

B. Mission with $\theta_s = 80°$

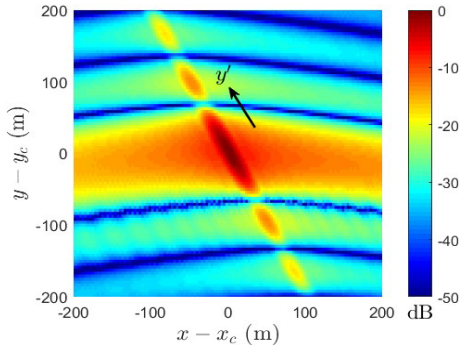

(a)

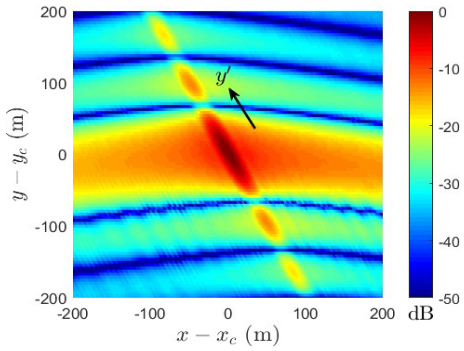

(b)

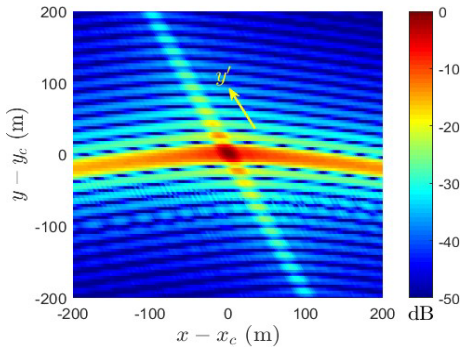

(c)

Fig. 11. Image reconstruction (a) with conventional RDA, $\theta_s = 80°$, $N_r = 16,384$, $N_a = 16,384$; (b) with RDA-based method in scheme C, $\theta_s = 80°$, $N'_r = 1,024$, $N'_a = 16,384$; (c) with RDA-based method in scheme D, $\theta_s = 80°$, $N'_r = 1,024$, $N'_a = 65,536$ [14].

Next, consider a scenario with the squit angle increased to $\theta_s = 80°$. Fig.11(a) shows the image reconstructed with the conventional RDA. Fig.11(b) shows the image reconstructed with the RDA-based method in scheme C, with $N'_r = 1,024$ and $N'_a = 16,384$. The number of azimuth samples in scheme C remains the same as $N'_a = N_a$, and that of range samples is only 1/16 that of the conventional RDA.

In scheme D, $N'_r = 1,024$ and $N'_a = 65,536$, the number of range samples remains the same as that in scheme C, while that of azimuth samples is increased by four folds. Fig.11(c) shows that the reconstructed image appears to have finer spatial resolution in the y' direction because the synthetic aperture length is increased by four times.

Table V lists the performance indices of SAR imaging in schemes C and D, with $\theta_s = 80°$. The image reconstructed in scheme C appears similar to that with the conventional RDA. However, the former takes only 7.8 % of NOMs and 1/16 of memory as compared to the latter. The spatial resolutions in the x direction with the conventional RDA and scheme D are similar, and the spatial resolution in the y' direction with the latter is only half that with the former. Scheme D takes 419 % of NOMs and four times of memory as compared to scheme C. However, the former takes only 33 % of NOMs and one quarter of memory as compared to the conventional RDA. In summary, the RDA-based method in scheme D outperforms the conventional RDA in the spatial resolution along y' direction, NOMs and memory.

TABLE V
PERFORMANCE INDICES OF SAR IMAGING, $\theta_s = 80°$ [14].

index	conventional	scheme C	scheme D
IRW_x (m)	17.3193	17.3099	17.4109
$\text{IRW}_{y'}$ (m)	66.3484	66.4359	16.3679
$\text{PSLR}_{y'}$ (dB)	-13.2816	-13.2475	-13.1884
NOM (million)	35,165	2,751	11,542
memory (GB)	4	0.25	1

IV. FDA-BASED METHOD

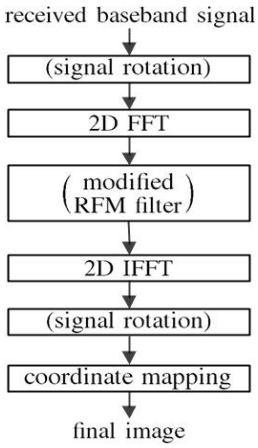

Fig. 12. Flowchart of FDA-based method for high-squint SAR imaging [17]. The processes enclosed with parentheses are different from those in the conventional FDA [20].

Fig.12 shows the flowchart of the FDA-based method for high-squint SAR imaging [17], and the processes different from those in the conventional FDA [20] are enclosed with parentheses. The received baseband signal is rotated in the τ-η plane before being Fourier transformed to the f_τ-f_η plane. The reference function multiply (RFM) filter is rotated in the f_τ-f_η plane by the same angle. Finally, the processed signal is reversely rotated in the τ-η plane to reconstruct the final image.

The slant range in a SAR mission can be represented as [20]

$$R_s(\eta) = |\bar{r}_s(\eta) - \bar{r}_g(\eta)| \tag{13}$$

where $\bar{r}_s(\eta)$ and $\bar{r}_g(\eta)$ are the positions of the satellite and the target, respectively, at azimuth time η. Define

$$\begin{aligned}
\bar{R}(\eta) &= \bar{r}_s(\eta) - \bar{r}_g(\eta) \\
\bar{V}(\eta) &= \frac{d\bar{R}(\eta)}{d\eta} = \bar{v}_s(\eta) - \bar{v}_g(\eta) \\
\bar{A}(\eta) &= \frac{d\bar{V}(\eta)}{d\eta} = \bar{a}_s(\eta) - \bar{a}_g(\eta) \\
\bar{B}(\eta) &= \frac{d\bar{A}(\eta)}{d\eta} = \bar{b}_s(\eta) - \bar{b}_g(\eta) \\
\bar{D}(\eta) &= \frac{d\bar{B}(\eta)}{d\eta} = \bar{d}_s(\eta) - \bar{d}_g(\eta) \\
\bar{E}(\eta) &= \frac{d\bar{D}(\eta)}{d\eta} = \bar{e}_s(\eta) - \bar{e}_g(\eta)
\end{aligned}$$

where $\bar{v}_s(\eta)$ and $\bar{v}_g(\eta)$ are the velocity vectors of the satellite and the target, respectively; $\bar{a}_s(\eta)$ and $\bar{a}_g(\eta)$ are the acceleration vectors of the satellite and the target, respectively; $\bar{b}_s(\eta)$ and $\bar{b}_g(\eta)$ are the time derivatives of $\bar{a}_s(\eta)$ and $\bar{a}_g(\eta)$, respectively; $\bar{d}_s(\eta)$ and $\bar{d}_g(\eta)$ are the time derivatives of $\bar{b}_s(\eta)$ and $\bar{b}_g(\eta)$, respectively; $\bar{e}_s(\eta)$ and $\bar{e}_g(\eta)$ are the time derivatives of $\bar{d}_s(\eta)$ and $\bar{d}_g(\eta)$, respectively; all at azimuth time η. The slant range can be represented in terms of a fifth-order Doppler parameter range model (DRM-5) as [20]

$$R_s(\eta) = R_c + \sum_{n=1}^{5} k_n \eta^n \tag{14}$$

where $R_c = |\bar{R}(0)|$ is the slant range at $\eta = 0$, and

$$\begin{aligned}
k_1 &= \frac{\bar{R}^t(0)\cdot\bar{V}(0)}{|\bar{R}(0)|} \\
k_2 &= \frac{\bar{R}^t(0)\cdot\bar{A}(0) + \bar{V}^t(0)\cdot\bar{V}(0) - k_1^2}{2|\bar{R}(0)|} \\
k_3 &= \frac{\bar{R}^t(0)\cdot\bar{B}(0) + 3\bar{V}^t(0)\cdot\bar{A}(0) - 6k_1k_2}{6|\bar{R}(0)|} \\
k_4 &= \frac{\bar{R}^t(0)\cdot\bar{D}(0) + 4\bar{V}^t(0)\cdot\bar{B}(0) + 3\bar{A}^t(0)\cdot\bar{A}(0)}{24|\bar{R}(0)|} \\
&\quad - \frac{k_2^2 + 2k_1k_3}{2|\bar{R}(0)|} \\
k_5 &= \frac{\bar{R}^t(0)\cdot\bar{E}(0) + 5\bar{V}^t(0)\cdot\bar{D}(0) + 10\bar{A}^t(0)\cdot\bar{B}(0)}{120|\bar{R}(0)|} \\
&\quad - \frac{k_2k_3 + k_1k_4}{|\bar{R}(0)|}
\end{aligned}$$

An RFM filter is devised as [20]

$$H_{\mathrm{RFM}}(f_\tau, f_\eta) = e^{-j[\phi_r(f_\tau)+\phi_{\mathrm{RCM}}(f_\tau,f_\eta)+\phi_a(f_\eta)+\phi_c(f_\tau,f_\eta)]} \tag{15}$$

where $\phi_r(f_\tau)$, $\phi_{\mathrm{RCM}}(f_\tau, f_\eta)$, $\phi_a(f_\eta)$ and $\phi_c(f_\tau, f_\eta)$ are the phases to implement range compression, range cell migration (RCM) correction, azimuth compression and decoupling, respectively. Their explicit forms are

$$\begin{aligned}
\phi_r(f_\tau) &= -\frac{\pi f_\tau^2}{K_r} \\
\phi_{\mathrm{RCM}}(f_\tau, f_\eta) &= -\frac{4\pi f_\tau}{c}\Big\{R_c \\
&\quad + \frac{\lambda_0^2 A_1}{8}\left[2f_{\mathrm{dc}}(f_\eta - f_{\mathrm{dc}}) + (f_\eta - f_{\mathrm{dc}})^2\right] \\
&\quad - \frac{\lambda_0^3 A_2}{24}\left[3f_{\mathrm{dc}}(f_\eta - f_{\mathrm{dc}})^2 + 2(f_\eta - f_{\mathrm{dc}})^3\right] \\
&\quad + \frac{\lambda_0^4 A_3}{64}\left[4f_{\mathrm{dc}}(f_\eta - f_{\mathrm{dc}})^3 + 3(f_\eta - f_{\mathrm{dc}})^4\right] \\
&\quad - \frac{\lambda_0^5 A_4}{160}\left[5f_{\mathrm{dc}}(f_\eta - f_{\mathrm{dc}})^4 + 4(f_\eta - f_{\mathrm{dc}})^5\right]\Big\} \\
\phi_a(f_\eta) &= -\frac{4\pi R_c}{\lambda_0} + \frac{\pi\lambda_0 A_1}{2}(f_\eta - f_{\mathrm{dc}})^2 \\
&\quad - \frac{\pi\lambda_0^2 A_2}{6}(f_\eta - f_{\mathrm{dc}})^3 + \frac{\pi\lambda_0^3 A_3}{16}(f_\eta - f_{\mathrm{dc}})^4 \\
&\quad - \frac{\pi\lambda_0^4 A_4}{40}(f_\eta - f_{\mathrm{dc}})^5 \\
\phi_c(f_\tau, f_\eta) &= \left(\frac{\pi f_\tau^2 f_\eta^2}{f_0^2}\right)\left\{\frac{\lambda_0 A_1}{2} - \frac{\lambda_0^2 A_2}{2}(f_\eta - f_{\mathrm{dc}})\right. \\
&\quad \left. + \frac{3\lambda_0^3 A_3}{8}(f_\eta - f_{\mathrm{dc}})^2 - \frac{\lambda_0^4 A_4}{4}(f_\eta - f_{\mathrm{dc}})^3\right\} \\
&\quad + \left(\frac{\pi f_\tau^3 f_\eta^2}{f_0^3}\right)\left\{-\frac{\lambda_0 A_1}{2} + \frac{\lambda_0^2 A_2}{6}\left[4(f_\eta - f_{\mathrm{dc}}) + f_{\mathrm{dc}}\right]\right. \\
&\quad - \frac{\lambda_0^3 A_3}{8}\left[5(f_\eta - f_{\mathrm{dc}})^2 + 2f_{\mathrm{dc}}(f_\eta - f_{\mathrm{dc}})\right] \\
&\quad \left. + \frac{\lambda_0^4 A_4}{4}\left[2(f_\eta - f_{\mathrm{dc}})^3 + f_{\mathrm{dc}}(f_\eta - f_{\mathrm{dc}})^2\right]\right\}
\end{aligned}$$

where

$$\begin{aligned}
A_1 &= \frac{1}{2k_2}, \quad A_2 = -\frac{3k_3}{8k_2^3}, \quad A_3 = \frac{9k_3^2 - 4k_2k_4}{16k_2^5} \\
A_4 &= -\frac{135k_3^3 - 120k_2k_3k_4 + 20k_2^2k_5}{128k_2^7}
\end{aligned}$$

The RFM filter is applied in the f'_τ-f'_η domain, with the form of

$$H_{\mathrm{RFM}}(f'_\tau, f'_\eta) = H_{\mathrm{RFM}}(f_\tau, f_\eta)\Big|_{f_\tau = g_1(f'_\tau, f'_\eta), f_\eta = h_1(f'_\tau, f'_\eta)} \tag{16}$$

TABLE VI
PARAMETERS OF TUNDRA ORBIT [16].

parameter	symbol	magnitude	unit
semi-major axis	a	42,164	km
eccentricity	e	0.3	
right of ascending node	Ω	40	deg.
orbital inclination	i	63.4	deg.
argument of perigee	ω	270	deg.
true anomaly	ν	180	deg.

A. Satellite Orbit and Ephemeris

Table VI lists the parameters of a Tundra orbit [16]. A constellation of two satellites are deployed to detect a point

target specified in the Earth-centered Earth-fixed (ECEF) coordinates. The right-of-ascending-node and the true anomaly of the second satellite differ from those of the first one by 180°, and the other parameters are the same.

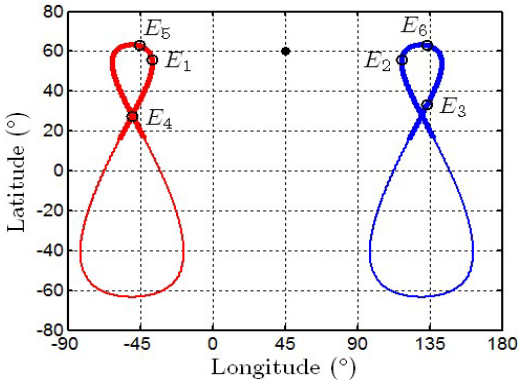

(a)

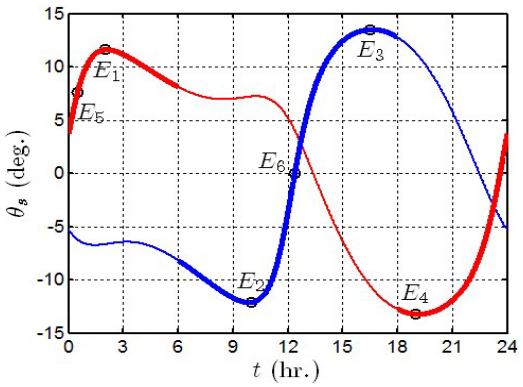

(b)

Fig. 13. (a) Ephemeris of two Tundra satellites, the solid circle marks a point target. (b) Time history of squint angles measured from two Tundra satellites [17].

Fig.13(a) shows the ephemeris of the two Tundra satellites. The solid circle marks a point target selected for simulation. Along each ephemeris, the thick part marks the working window, which is centered around the apogee and lasts for about half of the period. Fig.13(b) shows the time history of squint angles (θ_s) measured from each of the two Tundra satellites. The period of each Tundra satellite is $T = 24$ hours, and the first satellite passes the apogee at $t = 0$. In other words, the first satellite operates in $0 < t < T/4$ and $3T/4 < t < T$, and the second one operates in the rest of the period.

The SAR images of the target point are taken at six instants, marked as events E_1-E_6 in Fig.13. The four events E_1-E_4 involve high squint angles, event E_5 involves a small squint angle, and event E_6 involves zero squint angle. The conventional FDA is also applied to reconstruct images for comparison. Events E_1-E_4 impose more challenges than the other two events on applying the HEO satellites for SAR imaging.

TABLE VII
PARAMETERS OF GEO SAR MISSIONS [20].

parameter	symbol	magnitude	unit
carrier frequency	f_0	1.2	GHz
chirp pulse duration	T_r	50	μs
range chirp rate	K_r	620	GHz
bandwidth	B_r	31	MHz
range sampling rate	F_r	64 / 128*	MHz
range sampling interval	$\Delta\tau$	15.63 / 7.81*	ns
azimuth sampling rate	F_a	120 / 240*	Hz
azimuth sampling interval	$\Delta\eta$	8.33 / 4.17*	ms

a/b^*: a is used in Events E_1-E_4 and b is used in Events E_5, E_6.

B. *Event* E_1

Table VII lists the parameters of a GEO SAR mission [20], which are used for the HEO SAR simulations. The memories required by the conventional FDA and the FDA-based method to store the received signal are on the order of $N_r \times N_a$ and $N_r' \times N_a'$, respectively.

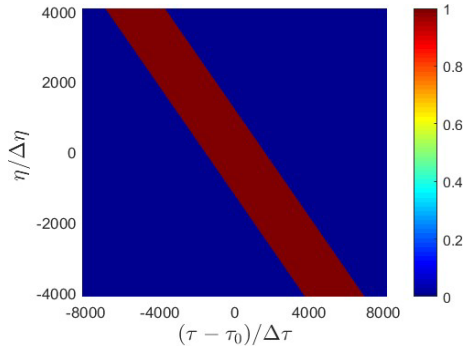

(a)

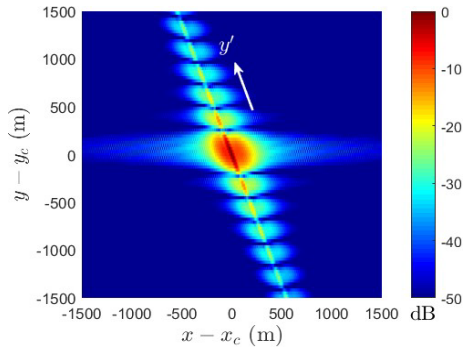

(b)

Fig. 14. (a) Received signal in τ-η plane and (b) image reconstructed with conventional FDA, $N_r = 16,384$, $N_a = 8,192$ [17].

Fig.14(a) shows the received signal in the τ-η plane, which is computed by using (1). Fig.14(b) shows the image reconstructed with the conventional FDA, in which local maxima are observed along the x axis and a y' axis.

Fig.15(a) shows the image reconstructed with the FDA-based method. Scheme A is formed by reducing the number of range samples from $N_r = 16,384$ to $N_r' = 4,096$, while keeping the number of azimuth samples as $N_a' = 8,192$. The reconstructed image appears similar to that with the conventional FDA.

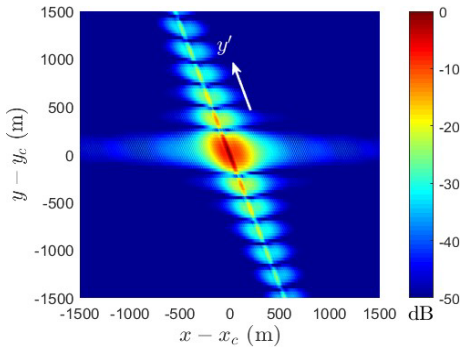

(a)

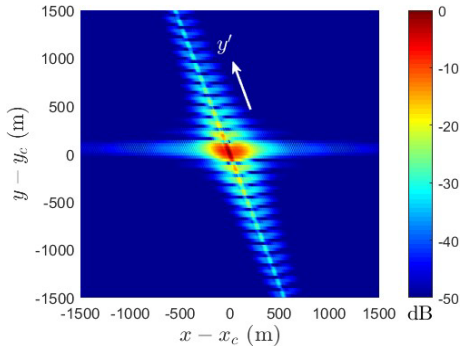

(b)

Fig. 15. Image reconstructed with FDA-based method, (a) scheme A, $N_r' = 4,096$, $N_a' = 8,192$, (b) scheme B, $N_r' = 4,096$, $N_a' = 16,384$ [17].

TABLE VIII
PERFORMANCE INDICES OF SAR IMAGING IN EVENT E_1 [17].

index	conventional	scheme A	scheme B
IRW$_x$ (m)	29.651	29.9558	30.6552
IRW$_{y'}$ (m)	220.0219	222.4984	112.075
PSLR$_{y'}$ (dB)	-13.2704	-13.2437	-13.2968
NOM (million)	15,166	4,932	10,133
memory (GB)	2	0.5	1

Scheme B is formed by choosing $N_r' = 4,096$ and increasing N_a' from 8,192 to 16,384. Thus, the NOMs and memory required in scheme B are larger than those in scheme A. Fig.15(b) shows the image reconstructed with scheme B. The number of range samples is only a quarter that of the conventional FDA, and the number of azimuth samples is twice that of the latter. The reconstructed image has finer spatial resolution in the y' direction because the synthetic aperture length is doubled.

Table VIII lists the performance indices of SAR imaging in event E_1. The images reconstructed with the conventional FDA and the FDA-based method in scheme A appear similar. However, the latter takes only 33 % of NOMs and 25 % of memory as compared to the former. The spatial resolutions in the x direction with both methods are similar; and the spatial resolution in the y' direction with the FDA-based method in scheme B is about half that with the conventional FDA. Scheme B takes 205 % of NOMs and twice memory as compared to scheme A. However, the former takes only 67 % of NOMs and one half of memory as compared to the conventional FDA. In summary, the FDA-based method in scheme B out-performs the conventional FDA in the spatial resolution along y' direction, NOMs and memory. The simulations in events E_2-E_4 demonstrate similar results.

TABLE IX
PERFORMANCE INDICES OF SAR IMAGING IN EVENT E_5 [17].

index	conventional	FDA-based
IRW$_x$ (m)	33.425	33.2845
PSLR$_x$ (dB)	-13.0985	-13.1341
IRW$_{y'}$ (m)	144.074	145.2704
PSLR$_{y'}$ (dB)	-13.2202	-13.2274
NOM (million)	31,407	20,803
memory (GB)	4	2

C. Event E_5

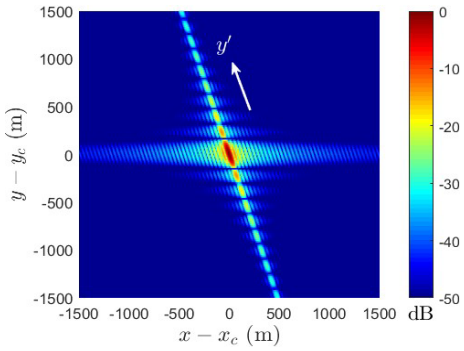

(a)

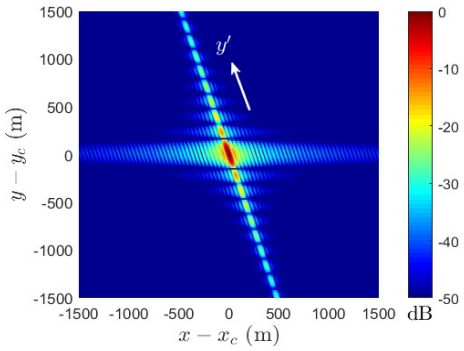

(b)

Fig. 16. Image reconstructed (a) with conventional FDA, $N_r = 16,384$, $N_a = 16,384$, (b) with FDA-based method, $N_r' = 8,192$, $N_a' = 16,384$ [17].

Fig.16(a) shows the image reconstructed with the conventional FDA, in which local maxima are observed along x and y' axes. Fig.16(b) shows the image reconstructed with the FDA-based method. The number of range samples is reduced from $N_r = 16,384$ to 8,192, while the number of azimuth samples remains as $N_a' = 16,384$. The image reconstructed with both methods have similar quality.

Table IX lists the performance indices of SAR imaging in event E_5. The FDA-based method takes only 66 % of NOMs and one half memory as compared to the conventional FDA.

V. SUMMARY

We have reviewed four modified chirp scaling algorithms (CSAs), one modified range-Doppler algorithm (RDA), and one modified frequency-domain algorithm (FDA), which are used to improve the quality of SAR imaging under high squint angles. Scenarios with squint angles up to 60° and 80° have been simulated to demonstrate the efficacy of these methods in terms of spatial resolution, computational load and memory size. Two HEO satellites in a Tundra orbit are envisioned for SAR imaging, which are capable of providing a complete coverage over high-latitude areas.

REFERENCES

[1] Q.-L. Zhai, W. Wang, J.-M. Hu, and J. Zhang, "Azimuth nonlinear chirp scaling integrated with range chirp scaling algorithm for highly squinted SAR imaging," *Prog. Electromag. Res.*, vol. 143, pp. 165 - 185, 2013.

[2] D.-X. An, Z.-M. Zhou, X.-T. Huang, and T. Jin, "A novel imaging approach for high resolution squinted spotlight SAR based on the deramping-based technique and azimuth NLS principle," *Prog. Electromag. Res.*, vol. 123, pp. 485 - 508, 2012.

[3] Y. Wu, G-C Sun, X.-G. Xia, M. Xing, J. Yang, and Z. Bao, "An azimuth frequency non-linear chirp scaling (FNCS) algorithm for TOPS SAR imaging with high squint angle," *IEEE J. Select. Topics Appl. Earth Observ. Remote Sensing*, vol. 7, no. 1, pp. 213 - 222, Jan. 2014.

[4] S. Chen, S.-I. Zhang, H.-C. Zhao, and Y. Chen, "A new chirp scaling algorithm for highly squinted missile-borne SAR based on FrFT," *IEEE J. Select. Topics Appl. Earth Observ. Remote Sensing*, vol. 8, no. 8, pp. 3977 - 3987, Aug. 2015.

[5] G.-G. Liu, P. Li, S.-Y. Tang, and L.-R. Zhang, "Focusing highly squinted data with motion errors based on modified non-linear chirp scaling," *IET Radar Sonar Navig.*, vol. 7, no. 5, pp. 568 - 578, Jun. 2013.

[6] D. Li, H. Lin, H.-Q. Liu, G.-S. Liao, and X.-H. Tan, "Focus improvement for high-resolution highly squinted SAR imaging based on 2-D spatial-variant linear and quadratic RCMs correction and azimuth-dependent Doppler equalization," *IEEE J. Select. Topics Appl. Earth Observ. Remote Sensing*, vol. PP, no. 99, pp. 1 - 16, Jun. 2016.

[7] P.-P. Huang, W. Xu, and S.-Y. Li, "Spaceborne squinted multichannel synthetic aperture radar data focusing," *IET Radar Sonar Navig.*, vol. 8, no. 9, pp. 1073 - 1080, Feb. 2015.

[8] H.-S. Shin and J.-T. Lim, "Range migration algorithm for airborne squint mode spotlight SAR imaging," *IET Radar Sonar Navig.*, vol. 1, no. 1, pp. 77 - 82, Feb. 2007.

[9] W. Li and J. Wang, "A new improved step transform algorithm for highly squint SAR imaging," *IEEE Geosci. Remote Sensing Lett.*, vol. 8, no. 1, pp. 118 - 122, Jan. 2011.

[10] Y. Tang, B. Zhang, M. Xing, Z. Bao, and L. Guo, "Azimuth overlapped subaperture algorithm in frequency domain for highly squinted synthetic aperture radar," *IEEE Geosci. Remote Sensing Lett.*, vol. 10, no. 4, pp. 692 - 696, Jul. 2013.

[11] D.-X. An, X.-T. Huang, T. Jin, and Z.-M. Zhou, "Extended two-step focusing approach for squinted spotlight SAR imaging," *IEEE Trans. Geosci. Remote Sensing*, vol. 50, no. 7, pp. 2889-3000, Jul. 2012.

[12] Y. Liang, Z.-Y. Li, L. Zeng, M.-D. Xing, and Z. Bao, "A high-order phase correction approach for focusing HS-SAR small-aperture data of high-speed moving platforms," *IEEE J. Select. Topics Appl. Earth Observ. Remote Sensing*, vol. 8, no. 9, pp. 4551 - 4561, Sep. 2015.

[13] P.-C. Chen and J.-F. Kiang, "Improved chirp scaling algorithms for SAR imaging under high squint angle," *IET Radar Sonar Navig.*, vol.11, 2017.

[14] P.-C. Chen and J.-F. Kiang, "An improved range-Doppler algorithm for SAR imaging at high squint angles," *Prog. Electromag. Res. M*, vol. 53, pp. 41-52, 2017.

[15] L. Wood, Y. Lou, and O. Olusola, "Revisiting elliptical satellite orbits to enhance the O3b constellation," https://arxiv.org/ftp/arxiv/papers /1407/1407.2521.pdf

[16] S. D. Ilcev, *Global Mobile Satellite Communications for Maritime, Land and Aeronautical Applications*, Springer, 2005.

[17] P.-C. Chen and J.-F. Kiang, "SAR imaging on HEO satellites with an improved frequency-domain algorithm," *Prog. Electromag. Res. M*, vol. 55, pp. 189-201, 2017.

[18] I. G. Cumming and F. H. Wong, *Digital Processing of Synthetic Aperture Radar Data*, Artech House, 2005.

[19] W. Wang, W.-H. Wu, W. Su, R.-H. Zhan, and J. Zhang, "High squint mode SAR imaging using modified RD algorithm," *IEEE China Summit Int. Conf. Signal Inform. Process.*, Beijing, China, pp. 589 - 592, Jul. 2013.

[20] B. Zhao, Y. Han, W. Gao, Y. Luo, and X. Han, "A new imaging algorithm for geosynchronous SAR based on the fifth-order Doppler parameters," *Prog. Electromagn. Res. B*, vol. 55, pp. 195-215, 2013.